Energy-Coupling Mechanisms Revealed through Simultaneous Keyhole Depth and Absorptance Measurements during Laser-Metal Processing

Troy R. Allen,[1,*] Wenkang Huang,[2] Jack R. Tanner,[3] Wenda Tan,[2] James M. Fraser,[1,†] and Brian J. Simonds[3,‡]

[1] *Department of Physics, Engineering Physics & Astronomy, Queen's University, 64 Bader Lane, Kingston, Ontario, Canada K7L 3N6*

[2] *Department of Mechanical Engineering, University of Utah, 1495 E 100 S, Salt Lake City, Utah 84112, USA*

[3] *Applied Physics Division, National Institute of Standards and Technology, 325 Broadway, Boulder, Colorado 80305, USA*

(Received 22 November 2019; revised manuscript received 20 April 2020; accepted 27 May 2020; published 29 June 2020)

The interaction between high-irradiance light and molten metal is the complex multiphysics phenomenon that underpins industrial processes such as laser-based additive manufacturing, welding, and cutting. One aspect that requires careful attention is the formation and evolution of vapor depressions, or keyholes, within the molten metal. The dynamic behavior of these depressions can dramatically change the number of laser-beam reflections and is therefore intrinsically linked to the instantaneous energy coupled into the system. Despite its importance, there is a severe lack of direct *in situ*, experimental evidence of this relationship, which creates challenges for those who aim to model or control laser-based manufacturing processes. In this work, we combine two simultaneous state-of-the-art real-time measurement techniques (inline coherent imaging and integrating-sphere radiometry) to confirm and explore the definite positive correlation between the highly dynamic vapor-depression geometry and laser energy absorptance. For irradiances resulting in vapor-depression formation ($\geq$0.49 MW/cm^2), we observe excellent correlation (0.86) between the instantaneous depth (down to 800 μm) and the absorptance (up to 0.92), directly demonstrating their interdependence. In the transition mode, an important regime for additive manufacturing, we observe temporary vapor-depression formation with concomitant changes in absorptance from 0.34 to 0.53. At higher irradiances, we detect stepwise increases in the absorbed laser power with a smoothly increasing keyhole depth, which is a real-time experimental observation of the effect of multiple reflections during laser-metal processing. The value of simultaneous depth and absorption measurements for predictive model validation is presented using ray-tracing simulations, which also confirm the absorption enhancement via incremental increases in the reflection count. This work provides insight into the underlying physics of laser-based metal manufacturing that is useful toward deterministic modeling and real-time process control.

DOI: 10.1103/PhysRevApplied.13.064070

I. INTRODUCTION

With advances of fiber and disk lasers, the application of lasers within the manufacturing industry has grown rapidly in recent years. Focused laser beams can precisely apply energy to a confined region, which makes them well suited for fusion applications such as welding and three-dimensional (3D) metal additive manufacturing (AM) and for material-removal applications such as laser cutting. With sufficiently high laser irradiance, vaporization of liquid metal can lead to the formation of vapor depressions. These are cavities in the melt pool created when an evaporation recoil pressure first pushes liquid metal down, then eventually up and away from the point of laser contact [1]. Commonly referred to as keyholes, vapor depressions can extend deep into the material and allow the laser beam to scatter multiple times—greatly increasing the instantaneous energy coupled into the material [2–6]. This makes them generally desirable in laser-metal processing, where the reflectance of flat metal surfaces is in excess of 60% [7,8], and specifically desirable in laser welding applications for their ability to fuse metal parts together up to tens of millimeters deep [9–12]. However, the instability of keyholes can lead to sudden collapses of the cavity walls that can trap vapor, causing deleterious porosity in the solidified metal [13]. Furthermore, the high recoil pressure that creates and sustains these keyholes can lead to frequent violent ejection of liquid metal, leaving spatter on

*troy.allen@queensu.ca
†james.fraser@queensu.ca
‡brian.simonds@nist.gov

the surrounding virgin-metal surface and causing underfill of the fusion zone. This is of particular concern in laser-based metal powder AM, as ejecta landing on nearby unsintered powder and the formation of pores can compromise the integrity of the final part [14–16]. For these reasons, deep narrow keyhole formation is generally detrimental to the AM process [15] and good AM process parameters typically correspond to the formation of a shallow low-aspect-ratio vapor depression [17,18]. In practice, however, frequent changes in laser scan velocity make it difficult to maintain desirable conditions for all times during laser illumination [19]. The formation and evolution of vapor depressions is integral to laser-metal manufacturing and its understanding and precise control is crucial to ensuring high final part quality and widespread industry implementation.

The difficulty in understanding and controlling vapor depressions comes from the complex underlying physics and the inherent opacity of the system. In the tightly confined area surrounding the laser-metal interaction, there is a steep temperature gradient leading to a rapid transition from solid to liquid to vaporized metal. The result is a dynamic volume of liquid metal behaving under an unstable balance of surface-tension pressure (also called Laplace pressure), hydrodynamic pressure, and vaporization-recoil pressure [1,20,21]. The complexity increases once vapor depressions are formed. The change in geometry allows multiple scattering of the laser beam, dramatically changing the amount of laser power being coupled into the metal. Efforts to describe this system analytically or computationally usually employ strategic simplifications with a goal of matching a final simulated output to specific experimental results with high computational efficiency. This includes limited consideration of transient behavior and therefore gives no valuable insight into how to control the process in real time and cannot accurately predict the formation of defects. These problems could be overcome with the development of models that focus on time dynamics rather than static or steady-state outputs but this task is impeded by a lack of precise time-resolved experimental data for the validation of such models [12,22,23].

Recent work toward understanding energy coupling into a metal work piece has been performed using integrating-sphere radiometry (ISR) to measure the absolute absorptance of laser light during stationary illumination of a metal [6,24–27]. Time-resolved measurements have not only confirmed the expected rise in absorptance for increasing laser irradiance but have also observed and quantified important dynamic features such as the energy required to melt, the energy required to form vapor depressions, and periodic oscillations in the laser absorptance [6]. Simonds *et al.* have inferred that many of the features observed in the laser-absorptance data are a result of melt-pool dynamics, especially the formation of vapor depressions. *Ex situ* cross sections of the welds have provided useful estimates for the final keyhole depth and melt-pool extent and have historically been the standard method for such measurements but are destructive and not time resolved. In other work, high-speed video has been employed to observe and characterize real-time melt-pool behavior and the formation of denudation zones but primarily monitors only the metal surface [28,29]. Very recent progress in x-ray imaging has captured real-time melt-pool fluid flow and two-dimensional profiles of vapor-depression formation and evolution but is limited by strict sample requirements and the availability of synchrotron light sources [17,18,30–34]. Finally, inline coherent imaging (ICI) is a method that can directly measure melt-pool morphology and vapor-depression depth. ICI exploits low-coherence interferometry to perform high-speed measurements of the position of the metal surface using the same lens that focuses the high-power laser beam. It has been integrated with laser processing systems and has successfully measured keyhole depth in welding and performed defect detection in AM [35–39].

In this work, we observe the definite positive correlation between the highly dynamic keyhole geometry and laser energy absorptance using two simultaneous state-of-the-art real-time measurement techniques (ICI and ISR). The origins for temporal features observed in previous time-resolved absorptance data are clarified by direct measurements of the vapor-depression depth. The combined data, along with ray-tracing simulations, are used to provide an analysis of vapor-depression formation and evolution, dynamic energy coupling, and the intrinsic relationship between them. While the stationary experiments explored here do not use a scanned cw laser beam (like most industrial laser-based manufacturing processes), the conditions at the start of laser illumination will be similar for most processes, with the common factor being the formation of a vapor depression. This is particularly true for low scan speeds [39] and pulsed-laser applications involving repeated vapor-depression formation. Additionally, recent analytical modeling has shown that stationary laser-metal processing experiments can confirm transient scanned keyhole behavior [40]. The results presented here provide insight into the complex underlying physics of intense laser-metal processing, which will be valuable for the future development of process control and validation of models and simulations for laser welding and laser-based additive manufacturing.

II. METHODS

A. Processing laser

High-irradiance stationary laser illumination is performed using a 1-kW Yb-doped fiber laser with a 100-μm core delivery fiber. A 150-mm focusing optic is used to focus the processing laser beam to a $1/e^2$ spot size of

238 μm. The focused beam has an M^2 value of 9.8 and a Rayleigh length of 4.23 mm. In this experiment, the laser is operated with average powers ranging from 100 W to 410 W, confirmed to within 3% with a commercial power meter. Pulse irradiance is calculated from the average power and the area of the beam incidence using the $1/e^2$ diameter. The laser is fired in pulsed mode to produce single pulses of 10-ms nominal duration. The actual pulse durations range from 9.896 ms to 9.972 ms depending on the laser power setting. The temporal distributions of the laser pulses are top hat in nature, with rise times faster than 75 μs.

B. Inline coherent imaging

ICI is an interferometric measurement technique based on low-coherence interferometry. Imaging light from a broadband source is coupled into a fiber-based Michelson interferometer, where the sample arm is coupled into free space and combined coaxially with a processing laser, and the reference arm is coupled into free space and reflected off a flat mirror. During laser processing of metals, imaging light from the sample arm scatters off the metal sample at the point of processing laser incidence and is recombined with the reference-arm light. The recombined light is sent to a line-camera spectrometer, which analyses the interference pattern and extracts the height of the sample. ICI has been successfully applied to laser welding as a monitoring and quality-control tool, most notably to measure keyhole depth *in situ* [35–39]. In previous work, excellent agreement has been found between *in situ* ICI depth measurements and *ex situ* cross-section measurements [39,41].

The system used in this work uses a superluminescent diode with a center wavelength of 841 nm, a bandwidth of 32 nm, and nominal output power of 15 mW after coupling into single-mode fiber. The sample-arm light is directed through a set of XY galvanometers and then combined coaxially with the processing laser via a dichroic mirror. It is focused using the same optics as the processing laser, leading to a spot size of 49 μm, which defines the transverse resolution. The ICI system can extract sample height at a rate of 200 kHz, with an axial resolution of 15 μm (the minimum axial distance between two interfaces that can be distinguished) and a single-point measurement repeatability of 0.6 μm. A schematic of the ICI system is shown in Fig. 1.

C. Integrating-sphere radiometry

Real-time absorptance measurements are made using ISR. An integrating sphere is installed to collect and measure all off-axis light scattered from laser illumination. By comparing to the known laser power incident on the work piece, the absorptance can be calculated. The working principle and calibration method of the integrating sphere

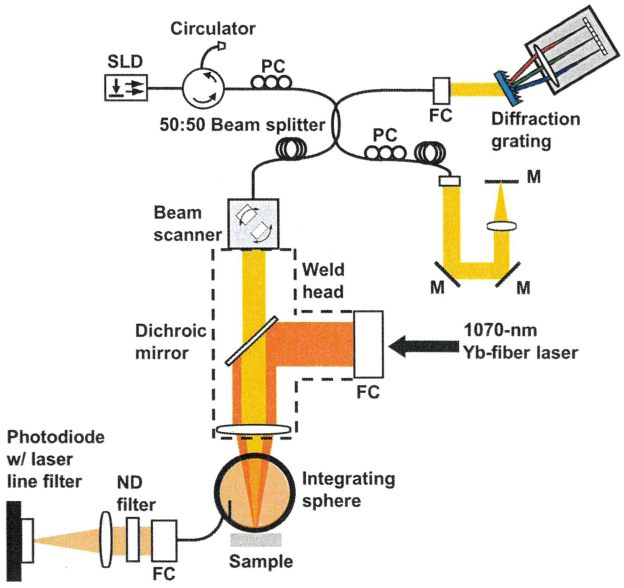

FIG. 1. The experimental setup, consisting of the inline coherent imaging system, the ISR system, and the processing laser: SLD, superluminescent diode; PC, polarization control; FC, fiber collimator; M, mirror; ND, neutral density.

is described in detail in recent work [6], so the description here will focus on differences in the current setup.

The sphere is 3D printed from black polylactic acid (PLA) in two hollow hemispheres. The bottom half includes a sample port with an aperture diameter of 5 mm, a fiber port with a ferrule connector–physical contact (FC-PC) adapter, a baffle to shield the fiber port from direct reflections, and a built-in mounting bracket. The top half includes the incoming light port, with a diameter of 7.5 mm. The as-printed interior surface of the hemispheres is rough and when coated with a flat white paint creates a diffuse reflective surface. This relatively simple coating is sufficient for these experiments, as we selectively measure light scattering at 1070 nm, so that spectral uniformity is not important. We also calibrate the loss factor of this coating before each laser shot, so any changes to the reflectivity of the inner surface are accounted for. When the halves are combined, the incoming light port at the top is in line with the sample port at the bottom. The interior diameter of the sphere is 76 mm.

A multimode fiber with a 400-μm core is connected to the FC-PC port on the sphere. A fraction of the light scattered inside the sphere is coupled into the fiber, which directs the light to a collimator and couples it back into free space. At this point, the light passes through a neutral-density (optical density 0.5) filter, which is removed in the calibration process. The light is then focused by a 100-mm lens onto an adjustable-gain silicon photodiode through a 1070-nm laser line filter. The rise time of the photodiode at the gain setting used in this work is 4.4 μs. The output of

the photodiode is read by an oscilloscope, which is controlled by a custom computer program. A schematic of the ISR system combined with the ICI system is shown in Fig. 1.

ISR typically includes a second photodiode inside the weld head, designed to measure any specular reflections of the processing laser exiting through the top of the sphere. Previous work has shown that signal measured by this photodiode is only relevant for a short time at the start of laser illumination and quickly drops to negligible levels [6]. The system used in the present work does not have such a photodiode, so the initial absorptance (when reflections are primarily specular) is not reported in the figures (for durations after laser turn-on of up to 400 μs).

D. Sample preparation

Samples of 316L stainless steel are prepared from NIST standard reference material (SRM) 1155a as in Ref. [6]. The only difference is that instead of washing with methanol, the samples are washed with a mild detergent solution before laser illumination. This SRM is chosen because high-temperature multiphase thermophysical properties have recently been measured on this specific metal-alloy composition, making this work more relevant for laser-process-model validation [42].

E. Ray-tracing model description

The simultaneous depth and absorptance measurements provide valuable data for laser-metal processing simulation validation, because they are *in situ* and in real time. As a demonstration, a 3D ray-tracing model is used to calculate the absorptance of the stationary laser-irradiance process. Since only one-dimensional depth is measured, the full keyhole shape used by the model is assumed from direct observations by high-speed x-ray imaging [17]. In the model, a laser beam with known power, spot size, and position is divided into a finite number of rays (178 000). As the rays travel into the keyhole, they are reflected multiple times until they escape. At each reflection, the laser power in the rays is partially absorbed by the keyhole wall. More complete details of the model are given in Refs. [2,43,44].

For each ray, the trajectory is explicitly tracked based on the assumption of linear ray transmission and the law of light reflection [2,45]:

$$\mathbf{R} = \mathbf{I} + 2(-\mathbf{I} \cdot \mathbf{N})\mathbf{N}, \tag{1}$$

where **N** is the unit vector of the surface-normal direction, **I** is the unit vector of the ray direction, and **R** is the unit vector of the reflected-ray direction. At each reflection, the laser power is absorbed into the keyhole wall based on the material's absorptivity and the overall absorptance can be calculated according to

$$A = \sum_{i}^{N} \sum_{j}^{M_i} p_{ij}\, \alpha(\theta_{ij}), \tag{2}$$

where A is the laser absorptance, N is the total number of rays, M_i is the ith ray's total reflection count in the keyhole, p_{ij} is the local laser power of the ith ray's jth reflection, and $\alpha(\theta_{ij})$ is the local Fresnel absorption coefficient of the ith ray's jth reflection. $\alpha(\theta)$ can be calculated for unpolarized light from [46]

$$\alpha(\theta) = 1 - \frac{1}{2}\left(\frac{1 + (1 - \epsilon\cos\theta)^2}{1 + (1 + \epsilon\cos\theta)^2}\right) - \frac{1}{2}\left(\frac{\cos^2\theta + (\epsilon - \cos\theta)^2}{\cos^2\theta + (\epsilon + \cos\theta)^2}\right), \tag{3}$$

where θ is the incident angle between **I** and **N** and ϵ is a material-dependent quantity defined by [47]

$$\epsilon^2 = \frac{2\epsilon_2}{\epsilon_1 + \left(\epsilon_1^2 + \left(\frac{1}{\omega\epsilon_0\rho}\right)^2\right)^{1/2}}, \tag{4}$$

where ϵ_1 and ϵ_2 are the real parts of the dielectric constants for the metal and the gas above it, respectively, ω is the angular frequency [$\omega = 2\pi c/\lambda$, where c is the speed of light and λ is the wavelength of the laser (1070 nm)], ϵ_0 is the vacuum permittivity, and ρ is the temperature-dependent electrical resistivity of AISI 316 stainless steel [48]. Thus, based on Eqs. (3) and (4), we can calculate the relationship between the Fresnel laser absorption coefficient and the incident angle for ANSI 316 stainless steel at its boiling temperature.

III. RESULTS AND DISCUSSION

A. Time-resolved vapor-depression depth and absorptance

Single laser pulses of 10 ms each are applied over a range of irradiance values that encompass conduction through keyhole-mode conditions (0.23–0.92 MW/cm^2). Figure 2 shows select time-resolved depth and absorptance data over this range. Note that a depth of 0 μm corresponds to the unirradiated metal surface, positive depth means that the surface is moving down into the work piece, and a negative depth is upwards toward the laser source. For a brief time at the start of laser illumination, most of the laser light reflects back into the weld head and is not collected by our ISR apparatus, making accurate measurements of absorptance impossible (see Sec. II C). This effect is short lived and quickly becomes negligible (as shown in Ref. [6]).

At low irradiance, shown in Fig. 2(a), the absorptance continuously rises from a minimum value of 0.30 to a

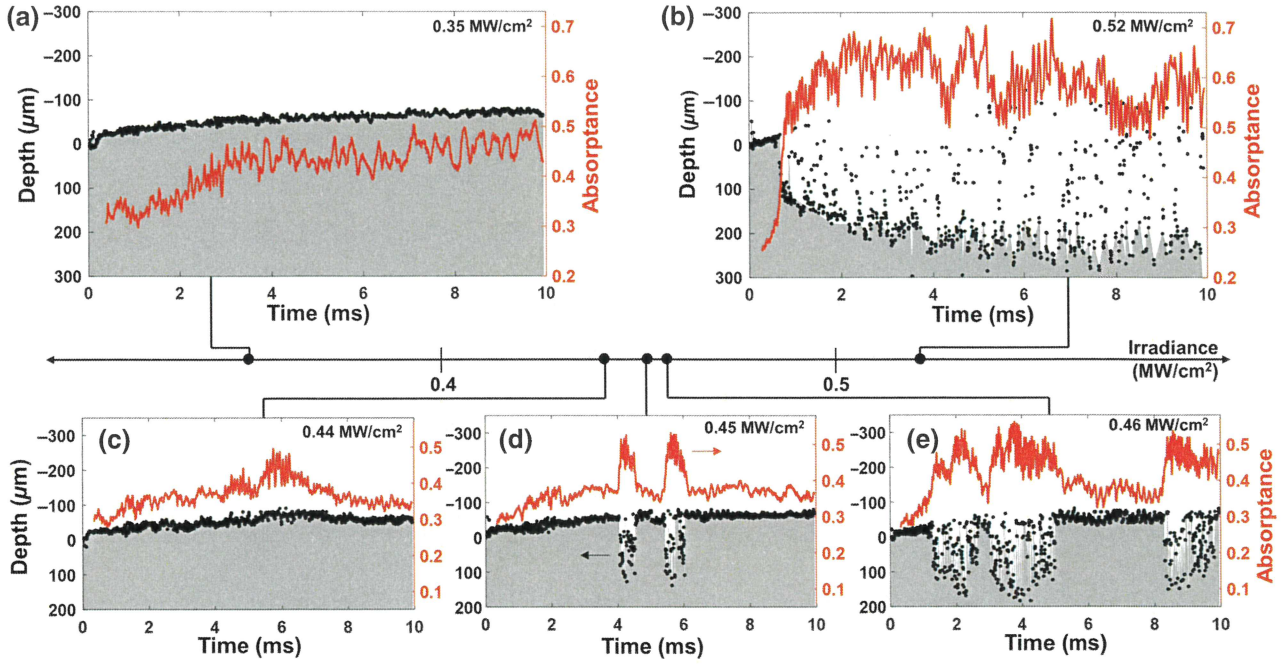

FIG. 2. The time-resolved depth and absorptance for incident irradiances ranging from 0.35 to 0.52 MW/cm^2 exhibiting behavior consistent with (a) the conduction mode, (b) the keyhole mode, and (c–e) the transition mode. The depth measurements are plotted against the left axis in black. The absorptance measurements are plotted against the right axis in red. The gray fill under the depth data is meant as a visual aid.

maximum value of 0.51 (red data, right ordinate). This is consistent with conductive heating of liquid steel and can be accounted for by a combination of the temperature dependence of absorptance [49,50] and the formation of oxides on the surface after melting [8,51]. The simultaneous depth measurements (black data, left ordinate) reveal a rising metal surface greater than 80 μm above the initial surface position. This is likely caused by a combination of local thermal expansion of the metal sample (in both the heat-affected solid and liquid melt pool) [42], as well as surface-tension pressure and fluid flow in the liquid melt pool [52]. The depth measurements confirm conductive heating by showing that no vapor depression is formed, corresponding to the laser beam reflecting only once off the surface.

At high irradiance [Fig. 2(b)], the absorptance is initially near 0.35, before it rapidly rises starting at 0.65 ms. This is followed by a period of frequent fluctuations around a mean value of 0.60, with minima and maxima of 0.48 and 0.72, respectively. Meanwhile, the metal surface initially rises for 0.640 ms. Then, there is a sudden increase in depth that is concurrent with the rapid increase in absorptance. Together, these data suggest that at this point in time, a vapor depression is formed and multiple reflections now dominate absorption. From this point until the end of laser illumination, the depth mostly tracks the bottom of the vapor depression from a depth of 100 μm to approximately 250 μm. Depth data points above the depression bottom are real, as we threshold our data to exclude signals with an intensity less than 12 dB above our noise floor. They likely result from fluctuations of the side walls, material being ejected from the keyhole, or partial collapses of the vapor depression itself. These forms of behavior have been observed by ultrahigh-speed *in situ* x-ray experiments [17,33]. Sporadic partial occlusion of the ICI beam is also supported by the absorptance data, as even though the depth appears to occasionally return to the surface, the absorptance remains relatively high, indicating that a significant vapor depression still exists.

The concurrent time-resolved depth and absorptance reveals keyhole instabilities in the transition region between the conduction and keyhole modes. An understanding of this region is important for manufacturing, as these instabilities can lead to porosity in laser welding and AM [19,53]. Data from the transition regime are shown in Figs. 2(c)–2(e) and are described in detail below:

2(c) At 0.44 MW/cm^2, the initial behavior of both the absorptance and the melt-surface position matches what is observed for the conduction mode. At 5.5 ms, both begin to oscillate rapidly, before decreasing over the last 3.5 ms. We believe that this change in behavior indicates the start of intense vaporization. The slight increase in depth is explained by the downward recoil force on the melt-pool surface overcoming surface-tension pressure and fluid-flow effects. The

reduction in absorptance can be explained by removal of oxides from the melt-pool surface by the increased vaporization [51].

2(d) At 0.45 MW/cm^2, we first see vapor-depression formation. For the first 4 ms, the behavior is consistent with the conduction mode. Then, the sample surface drops and there is a 40% relative increase in absorptance to over 0.5 due to vapor-depression formation. However, this is short lived as the increased energy input is not sufficient to sustain the depression against the surface-tension pressure [40]. After 540 μs, the depth and absorptance return to their predepression values, before the process is repeated less than 1 ms later. Repeated measurements at this irradiance level show similar behavior but with irregular timing of the vapor-depression formation and collapse.

2(e) At 0.46 MW/cm^2, temporary vapor depressions are formed more frequently, remain open longer, and reach slightly greater depths (maximum depth increased by 30 μm) and slightly higher absorptance values (maximum absorptance increased by 0.03).

These data show an unstable transition region before stable keyhole formation, which starts with the onset of vaporization and occurs over a narrow range of irradiance values. The hallmarks of this regime are a molten surface depth that can suddenly, but temporarily, plunge into the base metal with a simultaneous increase in absorbed laser power that tracks with depth. Further increases of irradiance eventually lead to a vapor depression that can be formed quickly and is maintained for the duration of laser illumination. This sustainable vapor-depression behavior, which we first observe at an irradiance of 0.49 MW/cm^2 (see Fig. S8 [54]), marks the beginning of the keyhole mode.

The keyhole mode is explored for higher irradiances in Fig. 3. Figure 3(a) shows time-resolved depth and absorptance data from incident irradiance of 0.92 MW/cm^2. Here, there is almost immediate formation of a vapor depression that grows smoothly and rapidly in depth along with a sharp increase in absorptance to over 0.8. This initial period, labeled "rapid growth," is defined by fitting the absorptance data to an exponential function and solving for the time at which the function reaches 97.5% of its steady-state value. Following the rapid-growth phase, which ends at 1.28 ms, the absorptance horizontally asymptotes and begins fluctuating around a mean value of 0.86. We label this region "steady state." The depth, meanwhile, continues to grow, albeit at a decreased rate, with increased instability.

The dual-regime keyhole behavior described above is applied to all data showing strong keyhole formation (irradiance values $\geq$0.58 MW/cm^2). Though these results are for stationary welds, similar behavior has been observed for moving welds at low scan speeds [39]. The depth from the rapid-growth regimes of these data are given in Fig. 3(b). Increased irradiances shorten the rapid-growth duration and increase the maximum depth achieved. This results from an increased vertical drilling rate, which we quantify for each regime by considering the initial and final depths. The drilling rate V_d is plotted in Fig. 3(c) as a function of the time-averaged absorbed irradiance I_{abs} for both regimes, where I_{abs} is equal to the regime's average absorptance times the applied irradiance. We model this as a linear dependence,

$$V_d = k(I_{\text{abs}} + C), \tag{5}$$

where k is a proportionality factor with units of m^3/J and C is a constant term related to the threshold of vapor-depression formation. The rapid-growth drilling rates range from 0.11 to 0.30 m/s, while the steady-state drilling rates are much lower (0.03–0.05 m/s). Both scale linearly, although the proportionality factor for the steady-state regime is an order of magnitude lower than the

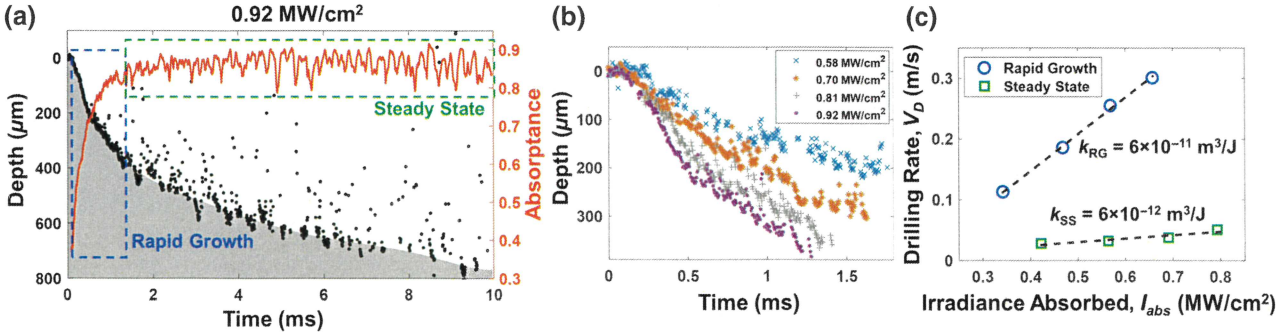

FIG. 3. (a) The time-resolved depth and absorptance from the keyhole mode (incident irradiance of 0.92 MW/cm^2). (b) Vapor-depression depth measurements during the rapid-growth period for four keyhole-mode trials of differing irradiances. (c) Drilling rates as a function of the average absorbed irradiance. The blue circles are drilling rates calculated during the rapid-growth period. The green squares are drilling rates calculated for the period of steady-state absorptance. The black dashed lines are linear fits to the data according to Eq. (5).

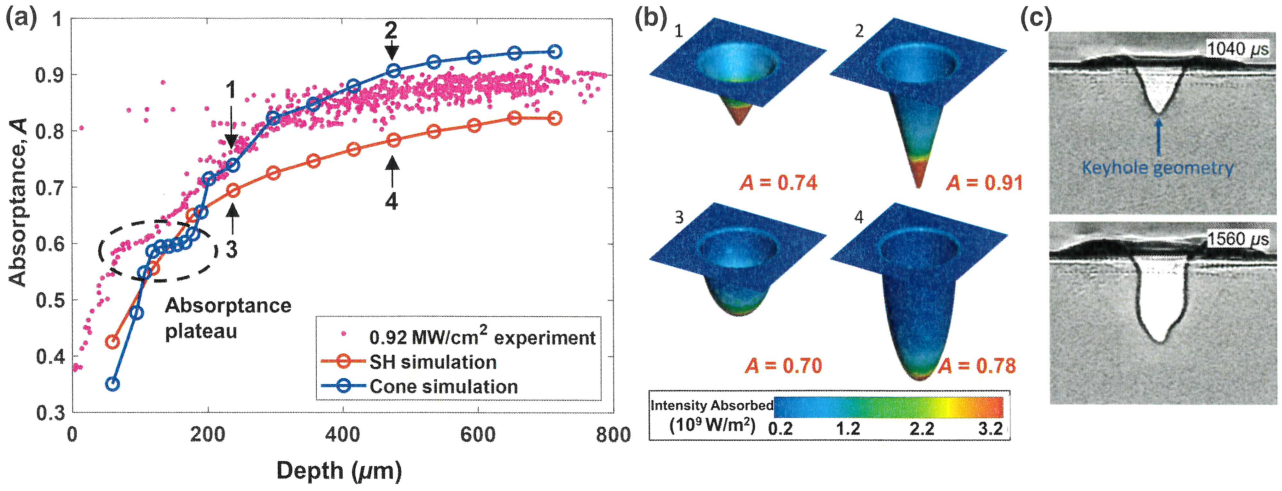

FIG. 4. (a) The absorptance and keyhole depth measured during laser irradiance of 0.92 MW/cm^2, compared to ray-tracing simulations. (b) The calculated absorbed laser power distribution on the keyhole wall and laser absorptance for depths of 238 μm (cases 1 and 3) and 476 μm (cases 2 and 4). (c) X-ray imaging shows a cone-shaped keyhole (top) and a SH-shaped keyhole (bottom) at different times during stationary laser illumination. From Ref. [17]. Reprinted with permission from AAAS.

rapid-growth regime ($k_{SS} = 6 \times 10^{12}$ m^3/J versus $k_{RG} = 6 \times 10^{11}$ m^3/J), despite consistently higher steady-state absorptance. The drilling becomes more difficult as the vapor depression grows larger, as viscous shear forces reduce outward flow momentum and hydrostatic pressure and surface-tension pressure increase downward melt flow back into the cavity [55]. A linear relationship between the drilling rate and the absorbed irradiance has been predicted previously [56] but under the assumption of constant absorbed irradiance. Here, we show that such a relationship exists but with different coefficients for two distinct growth regimes.

The dynamic relationship between the keyhole cavity depth and absorptance can also be explored by plotting the simultaneously obtained data against one another. This is shown in Fig. 4(a) for a strong keyhole condition (0.92 MW/cm^2) as a point cloud. The data increases asymptotically with the exception of a brief absorption plateau near 0.6 (circled on the figure). This plateau results from an increase in the number of multiple reflections from two to three, which only occurs after some critical cavity depth has been achieved. This is explored further in the next section using ray-tracing simulations. This data represents real-time experimental evidence of multiple reflections during laser-metal processing.

B. Model validation of vapor-depression depth and absorptance

The simultaneous high-speed measurement of melt-pool depth and laser absorptance presents a valuable opportunity to validate ray-tracing simulations. In this section, we demonstrate this capability while also exploring the previous experimental observation of real-time detection of multiple reflections. Ray-tracing simulations are used to calculate the laser power absorbed by keyholes of varying depth and geometry (Fig. 4). Our model relies on relevant material properties (see Sec. II E and Refs. [46–48]) and provides for an intuitive understanding of the results. Motivated by recent results from x-ray imaging [17], we consider the effects of cone-shaped and stretched-hemisphere- (SH) shaped cavities. The simulated depths range from 0 to 714 μm to match the experimental values and the radius of the opening of each keyhole is fixed to the $1/e^2$ radius of the incident laser beam (119 μm).

Figure 4(a) compares absorptance and depth measurements (point cloud) to simulation results (red and blue circles) for the two keyhole shapes over the same range of depths. Each simulation data point represents an independent ray-tracing calculation of the total absorptance A. Figure 4(b) shows example geometries and associated absorbed power distributions. Figure 4(c) shows images from ultrahigh-speed x-ray imaging experiments (performed at 200 kHz) [17], revealing a cone-shaped keyhole (top) and a SH-shaped keyhole (bottom) at different times during stationary laser illumination of metal. In both simulated geometries, the absorption is highest at the cavity bottom due to the higher intensity at the center of the laser beam (modeled as a Gaussian). A comparison of the experiment with the simulation results [Fig. 4(a)] reveals three important features: (1) both experiment and simulations follow the same trend—an asymptotic rise in absorptance with depth; (2) at large depths, a cone geometry predicts higher absorptance than the SH geometry, with the experimental results lying in between; and (3) the cone models recreate the experimentally observed absorptance plateau between 70 and 130 μm.

The first feature is consistent with analytical-model predictions for the emissivity of open cavities [57]. In general, this is a result of diminishing returns, as the more times a light ray is reflected, the less energy it has available for absorption. We calculate the average number of reflections and the remaining laser power in those rays and present this in the Supplemental Material (Fig. S14 [54]). Furthermore, this helps to explain the increased relative amplitude of the oscillations in the absorptance seen in the early stages of keyhole formation [Fig. 2(b)]. Since the keyhole depth is still relatively shallow, the average reflection count is small (1–3) and thus the absorptance is more sensitive to changes in depth.

Differences between the cone and SH models can also be understood in terms of the average number of keyhole-cavity reflections. These are determined for a 714-μm keyhole and are presented in the Supplemental Material (Fig. S15 [54]). At large depths (>700 μm), a cone-shaped geometry leads to, on average, many more reflections (8) versus the SH geometry (3–4) due to the differences in ray trajectories. In a cone-shaped keyhole, nearly all the reflected rays have the same angles of incidence and so a high-aspect-ratio cone results in a similar high number of reflections. For the SH geometry, the curved keyhole wall leads to a wider distribution of incident angles and therefore a wider distribution in reflection count. The fact that the experimental data lie between these two simulation results agrees with high-speed x-ray imaging of the stationary laser illumination process [17], which shows a fluctuating keyhole shape.

Lastly, we consider the offset between simulation and experiment at shallow depths and the plateau in absorptance observed in both the experimental and cone simulation results. In the early stages of keyhole formation, the absorptance is extremely sensitive to small changes in depth (i.e., there is a considerable increase in energy coupling as the system transitions from, on average, one to two reflections). Recall that ICI measures depth relative to the initial metal surface. Thus, the height of the liquid crown deposited around the keyhole opening, which effectively increases the depth [see Fig. 4(c)], is not accounted for. Since the simulations do not include a crown, they will systematically underestimate absorptance. Additionally, experimental geometries with a low reflection count will be disproportionately affected by side-wall perturbations that can locally increase the absorption. The simulations assume specular reflection from smooth surfaces and so will not include these contributions.

The temporary absorptance plateau that occurs despite increasing depth is captured with both experiment and cone-shaped simulations [see Fig. 4(a)]. This effect is the real-time manifestation of multiple reflections in a growing keyhole, as has been predicted by analytical models [4,58]. Figure 5(a) shows the absorptance and average reflection count calculated from the cone-shaped simulation, with both showing a plateau between 119 and 178 μm. At 119 μm, the angle of incidence for rays entering the keyhole is 45° and therefore every ray that enters the keyhole reflects twice before escaping [Fig. 5(b)]. As the depth increases, most rays will still escape the keyhole after two reflections until their trajectory is parallel to the opposite keyhole wall, which occurs at a depth of 164 μm. Once the depth increases beyond this threshold, some rays interact with the keyhole side wall a third time, as shown in green in Fig. 5(b) for a depth of 179 μm. Figure 5(c) shows the distribution of the reflection count within the keyhole for several depths near this threshold. For depths ranging from 119 to 155 μm, the majority of rays reflect twice and none reflect three times. At a depth of 179 μm, some reflect thrice, although the majority still reflect only twice. As the depth increases, a larger fraction of rays reflect three times and the plateau ends.

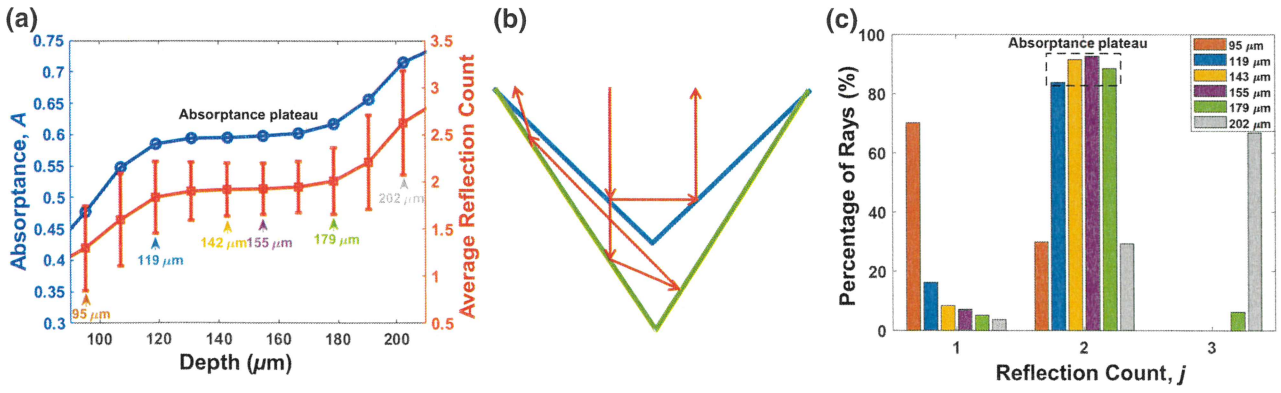

FIG. 5. (a) The absorptance and average reflection counts of rays for keyhole depths in and near the absorptance plateau for the cone-shaped simulation. The error bars represent the standard deviation of the average reflection count. (b) Schematic diagrams of ray trajectories for cone-shaped keyholes with depth of 119 μm (blue) and 179 μm (green). (c) The percentage of rays with reflection count j for the six keyhole depths marked in (a).

Since this behavior is not observed in the SH simulation results, it also suggests that the keyhole is initially more cone shaped. Smaller plateaus are predicted by simulation to occur at greater depths but their prominence is greatly reduced due to the diminishing returns in absorption increase discussed previously. This, along with the observed keyhole-shape fluctuations following the initial rapid-growth phase, hampers experimental observation of these higher-order plateaus.

C. Correlation between vapor-depression depth and absorptance

At high irradiances, larger vapor-depression depths corresponds to dramatically increased absorptance, while at low irradiance, the absence of a vapor depression results in a slow rise of both the melt-pool surface and absorptance. To quantify these phenomena, we calculate Spearman's rank correlation coefficient, ρ_s, between the two measurements for each irradiance value used in this experiment. Spearman's correlation assesses the degree to which two independent variables can be related by a monotonic function, that is, a function that either always increases ($\rho_s = +1$) or always decreases ($\rho_s = -1$). This approach is used because the absorptance can maximally only be 1 and thus a linear relationship required by other correlation analyses would be impossible. Figure 6(a) shows ρ_s for depth and absorptance plotted as a function of the irradiance, while Figs. 6(b)–6(d) show absorptance versus depth representative of each regime (conduction, transition, and keyhole, respectively).

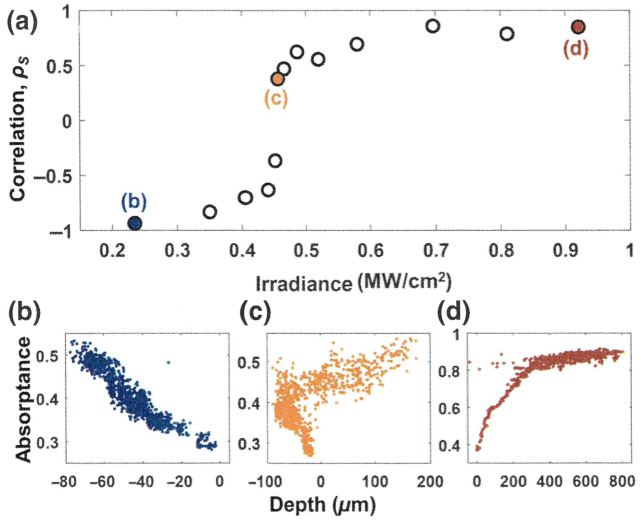

FIG. 6. (a) Spearman's rank correlation coefficient (ρ_s) for the depth and absorptance as a function of the incident irradiance. The colored points correspond to the like-colored plot below. The range of the error bars associated with these values is smaller than the size of the data markers. (b–d) Plots of the absorptance versus the depth for the conduction mode (0.23 MW/cm^2), the transition mode (0.46 MW/cm^2), and the keyhole mode (0.92 MW/cm^2), respectively. Note that the scales differ between each plot.

The keyhole mode (0.49–0.92 MW/cm^2) has a strong positive correlation, with $\rho_s > 0.55$, plateauing around 0.86. The plot for 0.92 MW/cm^2 [Fig. 6(d)] shows generally asymptotic behavior. In contrast, the conduction mode (0.23–0.41 MW/cm^2) has a strong negative correlation, with ρ_s ranging from -0.94 to -0.70. Negative values can be explained by time-resolved data, as we observe a decrease in depth (the sample surface rises) along with an increase in absorptance in this regime [see Fig. 2(a)]. Figure 6(b) shows that this relationship is not only monotonic but also linear. In the transition mode (0.44–0.47 MW/cm^2), the initial formation of a vapor depression causes ρ_s to rise sharply from -0.63 to 0.47. Figure 6(c) shows the characteristics of both the conduction and the keyhole modes, with negative depths having linear negative correlation and positive depths showing a positive monotonic relationship. This provides further evidence that the transition from the conduction to the keyhole mode exists across a narrow region of parameter space that shares the characteristics of both the conduction and the keyhole mode.

D. Time-averaged vapor-depression depth and absorptance

Previous works to quantify absorptance in laser material processing have calculated an average coupling efficiency over an entire weld duration [59–62]. We are able to calculate similar average values from the time-resolved data presented here. It is important to note, however, that exact thresholds for the conduction and keyhole modes determined from time-averaged coupling efficiency values will depend on the time duration, with shorter durations being more strongly affected.

Figure 7 shows time-averaged data from each irradiance value used in this experiment. The coupling efficiency is defined as the average absorptance over the duration of laser illumination (excluding early times as mentioned above) and the average depth is defined as the average of all depth measurements made over the same period. Average depth is used instead of maximum depth because it provides a more accurate measure of the influence of geometry (mainly vapor depressions) on the average coupling efficiency. For example, reporting the maximum depth measured for the transition-mode data shown in Fig. 2(d) would neglect the fact that a vapor depression is only formed for approximately 10% of the total duration and therefore overstate the expected geometric impact. The coupling efficiencies in the low-irradiance conduction regime fall within the expected range for single reflections off a liquid-steel surface [7]. At an irradiance of 0.45 MW/cm^2, the formation of temporary vapor

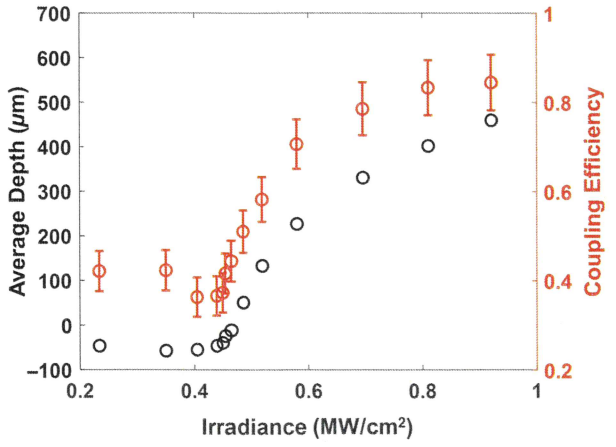

FIG. 7. The coupling efficiency (red, right ordinate) and average depth (black, left ordinate) plotted as a function of the incident irradiance. The error bars on the coupling efficiency are representative of a combination of systematic uncertainty and experimental repeatability. The standard error on average depth resulted in error bars smaller than the marker size.

depressions manifests as small increases in the coupling efficiency and average depth. With further increased irradiance, increases in the coupling efficiency are matched by increases in the average depth. This shows that both the coupling efficiency and the average depth can provide useful general insight for laser-metal processing applications.

E. Frequency-resolved vapor-depression depth and absorptance

The time-resolved data above reveal that the absorptance and the depth fluctuate even after the formation of deep vapor depressions, implying a complicated thermal evolution that is important to understand in order to predict the final microstructure [63,64]. These fluctuations in the dynamic absorptance and vapor-depression depth in the keyhole regime are analyzed by fast Fourier transforms (FFTs) to compare the oscillation frequency between the two independent measurements and to see how they both change with incident irradiance. Previously, it has been found that at the onset of the transition region between the conduction and the keyhole mode, there are peaks in frequency-resolved absorptance that agree with theoretical predictions for capillary waves of the melt pool [6], and that these peaks decrease in frequency with increasing irradiance (i.e., melt-pool size) [65,66]. In this work, we focus on the fluctuations of the measured vapor-depression depth during the keyhole mode and correlate these with fluctuations in absorptance.

Figure 8 shows frequency-resolved depth (bottom, black) and absorptance (top, red) data for the last 8 ms of laser illumination for three different irradiances within the keyhole regime. The sparse nature of the depth data requires linear interpolation in the regions of lost signal. The depth mean and standard deviation are also reported, as these quantities are related to the size of the melt pool and the amplitude of the depth oscillations, respectively. Visual inspection shows a clear correlation between the two individual measurements. At an irradiance of 0.49 MW/cm^2, on the lower edge of the keyhole mode, the peak frequency in both measured quantities is approximately 11 kHz. At 0.58 MW/cm^2, the peak frequency in both measured quantities is approximately 5 kHz. Finally, at 0.92 MW/cm^2, the peak frequency in both measured quantities is around 4 kHz. Over the same range, the mean measured depth grows from 60 to 569 μm, while the standard deviation is on the order of 100 μm in all cases. A decreasing fluctuation frequency as a function of an

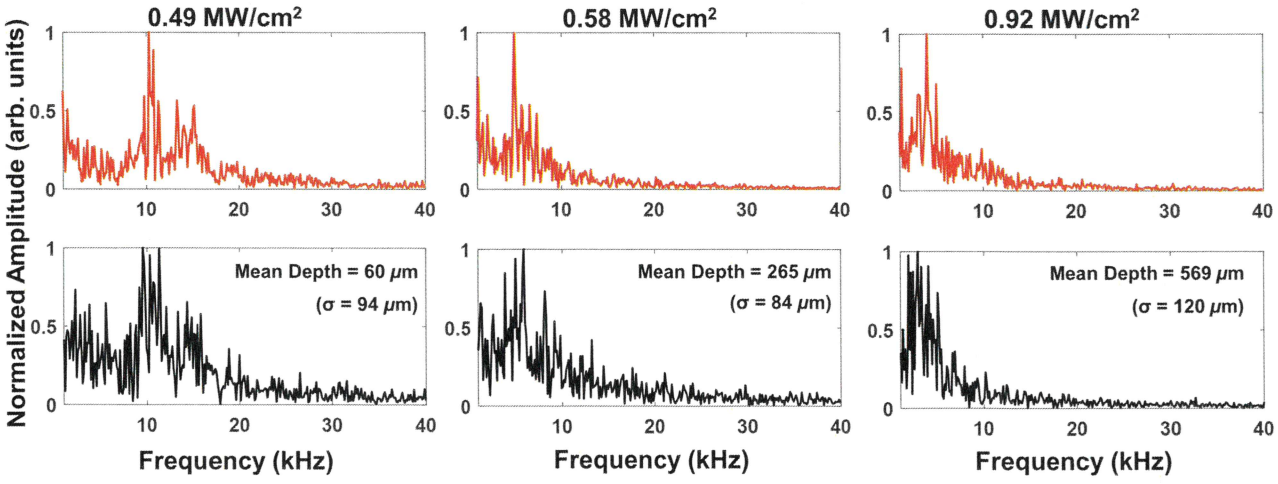

FIG. 8. The frequency-resolved depth (bottom) and absorptance (top) from the keyhole regime. FFTs are performed on data from the last 8 ms of laser illumination. The first 1 kHz is excluded from the plots, as this region is dominated by the dc term and by low-frequency contributions associated with initial vapor-depression formation.

increasing irradiance is consistent with lower oscillation frequencies for a larger melt-pool extent (represented by our measurements of higher average depth).

The correlation between the frequency components of the depth and absorptance demonstrates that there is a real quantifiable link between fluctuations in vapor-depression depth and instantaneous energy absorptance. In general, we observe that at higher irradiances, under relatively stable conditions, the relative amplitude of the absorptance oscillations is decreased but never eliminated. For instance, in the weak keyhole case in Fig. 2(b), with conditions relevant to AM, the absorptance oscillations after keyhole formation are approximately 17% of the mean value. For the strong keyhole case shown in Fig. 3(a), a comparable condition for laser welding, these oscillations in the steady-state regime are still as high as 5%. Therefore, computational models that aim to predict the resulting microstructure, either in AM or welding, but treat absorptance as a constant parameter could miss the effects of this potentially large and rapid fluctuation in instantaneous energy deposition.

IV. CONCLUSION

In summary, we observe and explore the definite positive correlation between the highly dynamic keyhole geometry and laser absorption using two simultaneous state-of-the-art real-time measurement techniques. We show that the conduction and keyhole modes can be clearly distinguished by their time-resolved signatures. This is done by observing the formation of vapor depressions, by both the increase in depth and by the associated increase in absorptance due to multiple reflections (to values greater than 0.9). The transition between these modes occurs over a narrow range of irradiance (0.44–0.47 MW/cm^2), where the frequency and duration of temporary vapor depressions are observed to increase until a consistent keyhole is formed at 0.49 MW/cm^2. If the irradiance is increased further, the keyhole mode develops an initial period of rapid growth in absorptance and depth, followed by steady-state behavior in absorptance and slow relatively unstable growth in depth. Distinguishing between these periods allows them to be considered separately in an exploration of keyhole growth and energy deposition over time. This reveals that the slope of the drilling rate as a function of the average absorbed irradiance decreases by an order of magnitude going from the rapid-growth regime to the steady-state regime. Fluctuations of absorptance and vapor-depression depth are shown to occur at similar frequencies (on the order of kilohertz) and scale together with the vapor-depression depth—demonstrating that even in strong keyhole mode, depth oscillations correlate with changes in the amount of energy absorbed. The experimental results lead to quantification of the relationship between the absorptance and the depth in the keyhole mode, allowing the comparison with ray-tracing simulations. This facilitates interpretation of the results in terms of keyhole geometry and the number of reflections they allow, revealing an incremental increase in the number of laser-beam reflections due to increasing vapor-depression depth. Thus, the effect of multiple reflections is experimentally observed in real time and quantified *in situ*. Overall, we show that energy coupling is highly sensitive to melt-pool geometry, especially in the early stages of keyhole formation, and it is therefore imperative for deterministic modeling that the treatment of absorptance moves beyond that of an unchanging constant of the material. The combined *in situ* monitoring methods used here can also act as a basis for future development of on-the-fly control for laser welding and laser-based-additive manufacturing processes.

ACKNOWLEDGMENTS

We thank Remy Fabbro [Procédés et Ingénierie en Mécanique et Matériaux (PIMM) Laboratory, Paris] and Nik Hrabe and Norman Sanford (both of NIST, Boulder, Colorado) for their careful reading of the manuscript and for insightful comments. W.H. and W.T. acknowledge the financial support from the National Science Foundation under Grant No. CMMI-1752218 and the technical support from the Center for High-Performance Computing at the University of Utah. T.R.A. and J.M.F. acknowledge funding received from the Natural Sciences and Engineering Research Council of Canada, the Canadian Foundation for Innovation, and the Ontario Centres of Excellence.

[1] V. Semak and A. Matsunawa, The role of recoil pressure in energy balance during laser materials processing, J. Phys. D: Appl. Phys. **30**, 2541 (1997).

[2] W. Tan, N. S. Bailey, and Y. C. Shin, Investigation of keyhole plume and molten pool based on a three-dimensional dynamic model with sharp interface formulation, J. Phys. D: Appl. Phys. **46**, 055501 (2013).

[3] A. Kaplan, A model of deep penetration laser welding based on calculation of the keyhole profile, J. Phys. D: Appl. Phys. **27**, 1805 (1994).

[4] S. C. Wang and P. S. Wei, Energy-beam redistribution and absorption in a drilling or welding cavity, Metall. Trans. B **23**, 505 (1992).

[5] C. Y. Ho and P. S. Wei, Energy absorption in a conical cavity truncated by spherical cap subject to a focused high-intensity beam, Int. J. Heat Mass Tran. **40**, 1895 (1997).

[6] B. J. Simonds, J. Sowards, J. Hadler, E. Pfeif, B. Wilthan, J. Tanner, C. Harris, P. Williams, and J. Lehman, Time-Resolved Absorptance and Melt Pool Dynamics during Intense Laser Irradiation of a Metal, Phys. Rev. Appl. **10**, 044061 (2018).

[7] D. Bergström, J. Powell, and A. F. H. Kaplan, The absorptance of steels to Nd:YLF and Nd:YAG laser light at room temperature, Appl. Surf. Sci. **253**, 5017 (2007).

[8] H. Kwon, W. K. Baek, M. S. Kim, W. S. Shin, and J. J. Yoh, Temperature-dependent absorptance of painted aluminum, stainless steel 304, and titanium for 1.07 and 10.6 μm laser beams, Opt. Laser Eng. **50**, 114 (2012).

[9] J. Kroos, U. Gratzke, and G. Simon, Towards a self-consistent model of the keyhole in penetration laser beam welding, J. Phys. D: Appl. Phys. **26**, 474 (1993).

[10] J. Dowden, M. Davis, and P. Kapadia, Some aspects of the fluid dynamics of laser welding, J. Fluid Mech. **126**, 123 (1983).

[11] D. T. Swift-Hook and A. E. F. Gick, Penetration welding with lasers, Weld. J. **52**, 492 (1973).

[12] J. Svenungsson, I. Choquet, and A. F. H. Kaplan, Laser welding process—A review of keyhole welding modelling, Phys. Procedia **78**, 182 (2015).

[13] S. Katayama, Y. Kawahito, and M. Mizutani, Elucidation of laser welding phenomena and factors affecting weld penetration and welding defects, Phys. Procedia **5**, 9 (2010).

[14] B. Zhang, Y. Li, and Q. Bai, Defect formation mechanisms in selective laser melting: A review, Chin. J. Mech. Eng. **30**, 515 (2017).

[15] S. A. Khairallah, A. T. Anderson, A. Rubenchik, and W. E. King, Laser powder-bed fusion additive manufacturing: Physics of complex melt flow and formation mechanisms of pores, spatter, and denudation zones, Acta Mater. **108**, 36 (2016).

[16] Y. Liu, Y. Yang, S. Mai, D. Wang, and C. Song, Investigation into spatter behavior during selective laser melting of AISI 316L stainless steel powder, Mater. Des. **87**, 797 (2015).

[17] R. Cunningham, C. Zhao, N. Parab, C. Kantzos, J. Pauza, K. Fezzaa, T. Sun, and A. D. Rollett, Keyhole threshold and morphology in laser melting revealed by ultrahigh-speed x-ray imaging, Science **363**, 849 (2019).

[18] S. M. H. Hojjatzadeh, N. D. Parab, W. Yan, Q. Guo, L. Xiong, C. Zhao, M. Qu, L. I. Escano, X. Xiao, K. Fezzaa, W. Everhart, T. Sun, and L. Chen, Pore elimination mechanisms during 3D printing of metals, Nat. Commun. **10**, 3088 (2019).

[19] A. A. Martin, N. P. Calta, S. A. Khairallah, J. Wang, P. J. Depond, A. Y. Fong, V. Thampy, G. M. Guss, A. M. Kiss, K. H. Stone, C. J. Tassone, J. Nelson Weker, M. F. Toney, T. van Buuren, and M. J. Matthews, Dynamics of pore formation during laser powder bed fusion additive manufacturing, Nat. Commun. **10**, 1987 (2019).

[20] V. V. Semak, J. A. Hopkins, M. H. McCay, and T. D. McCay, Melt pool dynamics during laser welding, J. Phys. D: Appl. Phys. **28**, 2443 (1995).

[21] J. Zhou, H.-L. Tsai, and P.-C. Wang, Transport phenomena and keyhole dynamics during pulsed laser welding, J. Heat Transfer **128**, 680 (2005).

[22] M. M. Francois *et al.*, Modeling of additive manufacturing processes for metals: Challenges and opportunities, Curr. Opin. Solid State Mater. Sci. **21**, 198 (2017).

[23] B. Schoinochoritis, D. Chantzis, and K. Salonitis, Simulation of metallic powder bed additive manufacturing processes with the finite element method: A critical review, Proc. Inst. Mech. Eng. B **231**, 96 (2015).

[24] C. Sainte-Catherine, M. Jeandin, D. Kechemair, J.-P. Ricaud, and L. Sabatier, Study of dynamic absorptivity at 10.6 μm (CO_2) and 1.06 μm (Nd:YAG) wavelengths as a function of temperature, J. Phys. IV **1**, C7151 (1991).

[25] R. Fabbro, S. Slimani, F. Coste, and F. Briand, Study of keyhole behaviour for full penetration Nd:YAG CW laser welding, J. Phys. D: Appl. Phys. **38**, 1881 (2005).

[26] J. T. Norris, C. V. Robino, M. J. Perricone, and D. A. Hirschfeld, Development of a time-resolved energy absorption measurement technique for laser beam spot welds, Weld. J. **89**, 75 (2010).

[27] C. Robino, Engineering approximations in welding: Bridging the gap between speculation and simulation, Weld. J. **95**, 1s (2016).

[28] J. Stavridis, A. Papacharalampopoulos, and P. Stavropoulos, Quality assessment in laser welding: A critical review, Int. J. Adv. Manuf. Technol. **94**, 1825 (2018).

[29] S. K. Everton, M. Hirsch, P. Stravroulakis, R. K. Leach, and A. T. Clare, Review of *in-situ* process monitoring and *in-situ* metrology for metal additive manufacturing, Mater. Des. **95**, 431 (2016).

[30] C. L. A. Leung, S. Marussi, R. C. Atwood, M. Towrie, P. J. Withers, and P. D. Lee, *In situ* x-ray imaging of defect and molten pool dynamics in laser additive manufacturing, Nat. Commun. **9**, 1355 (2018).

[31] C. Zhao, K. Fezzaa, R. W. Cunningham, H. Wen, F. De Carlo, L. Chen, A. D. Rollett, and T. Sun, Real-time monitoring of laser powder bed fusion process using high-speed x-ray imaging and diffraction, Sci. Rep. **7**, 3602 (2017).

[32] S. J. Wolff, H. Wu, N. Parab, C. Zhao, K. F. Ehmann, T. Sun, and J. Cao, *In-situ* high-speed x-ray imaging of piezo-driven directed energy deposition additive manufacturing, Sci. Rep. **9**, 962 (2019).

[33] C. Zhao, Q. Guo, X. Li, N. Parab, K. Fezzaa, W. Tan, L. Chen, and T. Sun, Bulk-Explosion-Induced Metal Spattering during Laser Processing, Phys. Rev. X **9**, 021052 (2019).

[34] A. A. Martin, N. P. Calta, J. A. Hammons, S. A. Khairallah, M. H. Nielsen, R. M. Shuttlesworth, N. Sinclair, M. J. Matthews, J. R. Jeffries, T. M. Willey, and J. R. I. Lee, Ultrafast dynamics of laser-metal interactions in additive manufacturing alloys captured by *in situ* x-ray imaging, Mater. Today Adv. **1**, 100002 (2019).

[35] J. A. Kanko, A. P. Sibley, and J. M. Fraser, *In situ* morphology-based defect detection of selective laser melting through inline coherent imaging, J. Mater. Process. Technol. **231**, 488 (2016).

[36] P. J. L. Webster, L. G. Wright, K. D. Mortimer, B. Y. Leung, J. X. Z. Yu, and J. M. Fraser, Automatic real-time guidance of laser machining with inline coherent imaging, J. Laser Appl. **23**, 022001 (2011).

[37] P. J. DePond, G. Guss, S. Ly, N. P. Calta, D. Deane, S. Khairallah, and M. J. Matthews, *In situ* measurements of layer roughness during laser powder bed fusion additive manufacturing using low coherence scanning interferometry, Mater. Des. **154**, 347 (2018).

[38] T. G. Fleming, S. G. Nestor, T. R. Allen, M. A. Boukhaled, N. J. Smith, and J. M. Fraser, Tracking and controlling the morphology evolution of 3D powder-bed fusion *in situ*

using inline coherent imaging, Addit. Manuf. **32**, 100978 (2020).

[39] J. J. Blecher, C. M. Galbraith, C. Van Vlack, T. A. Palmer, J. M. Fraser, P. J. L. Webster, and T. DebRoy, Real time monitoring of laser beam welding keyhole depth by laser interferometry, Sci. Technol. Weld. Joining **19**, 560 (2014).

[40] R. Fabbro, Depth dependence and keyhole stability at threshold, for different laser welding regimes, Appl. Sci. **10**, 1487 (2020).

[41] P. J. L. Webster, L. G. Wright, Y. Ji, C. M. Galbraith, A. W. Kinross, C. Van Vlack, and J. M. Fraser, Automatic laser welding and milling with *in situ* inline coherent imaging, Opt. Lett. **39**, 6217 (2014).

[42] P. Pichler, B. J. Simonds, J. W. Sowards, and G. Pottlacher, Measurements of thermophysical properties of solid and liquid NIST SRM 316L stainless steel, J. Mater. Sci. **55**, 4081 (2020).

[43] W. Tan and Y. C. Shin, Analysis of multi-phase interaction and its effects on keyhole dynamics with a multi-physics numerical model, J. Phys. D: Appl. Phys. **47**, 345501 (2014).

[44] W. Tan and W. Huang, in *Volume 2: Materials; Joint MSEC-NAMRC-Manufacturing USA* (ASME, 2018), p. V002T04A043.

[45] H. Ki, P. S. Mohanty, and J. Mazumder, Multiple reflection and its influence on keyhole evolution, J. Laser Appl. **14**, 39 (2002).

[46] R. Ducharme, K. Williams, P. Kapadia, J. Dowden, B. Steen, and M. Glowacki, The laser welding of thin metal sheets: An integrated keyhole and weld pool model with supporting experiments, J. Phys. D: Appl. Phys. **27**, 1619 (1994).

[47] J.-H. Cho and S.-J. Na, Implementation of real-time multiple reflection and Fresnel absorption of laser beam in keyhole, J. Phys. D: Appl. Phys. **39**, 5372 (2006).

[48] C. Y. Ho and T. K. Chu, Technical Report, Center for Information and Numerical Data Analysis and Synthesis, West Lafayette, Indiana, 1977.

[49] S. Boyden and Y. Zhang, Temperature and wavelength-dependent spectral absorptivities of metallic materials in the infrared, J. Thermophys. Heat Transfer **20**, 9 (2006).

[50] T. J. Wieting and J. L. Derosa, Effects of surface condition on the infrared absorptivity of 304 stainless steel, J. Appl. Phys. **50**, 1071 (1979).

[51] J. Xie and A. Kar, Laser welding of thin sheet steel with surface oxidation, Weld. J. **78**, 343 (1999).

[52] A. Paul and T. Debroy, Free surface flow and heat transfer in conduction mode laser welding, Metall. Trans. B **19B**, 851 (1988).

[53] M. Bayat, A. Thanki, S. Mohanty, A. Witvrouw, S. Yang, J. Thorborg, N. S. Tiedje, and J. H. Hattel, Keyhole-induced porosities in Laser-based Powder Bed Fusion (L-PBF) of Ti-6Al-4V: High-fidelity modelling and experimental validation, Addit. Manuf. **30**, 100835 (2019).

[54] See the Supplemental Material at http://link.aps.org/supplemental/10.1103/PhysRevApplied.13.064070 for time-resolved data from each irradiance value used in this work and additional ray-tracing results.

[55] J. Y. Lee, S. H. Ko, D. F. Farson, and C. D. Yoo, Mechanism of keyhole formation and stability in stationary laser welding, J. Phys. D: Appl. Phys. **35**, 1570 (2002).

[56] R. Fabbro and K. Chouf, Keyhole modeling during laser welding, J. Appl. Phys. **87**, 4075 (2000).

[57] T. J. Quinn, The calculation of the emissivity of cylindrical cavities giving near black-body radiation, Br. J. Appl. Phys. **18**, 1105 (1967).

[58] P. Solana and G. Negro, A study of the effect of multiple reflections on the shape of the keyhole in the laser processing of materials, J. Phys. D: Appl. Phys. **30**, 3216 (1997).

[59] P. W. Fuerschbach, Measurement and prediction of energy transfer efficiency in laser beam welding, Weld. J. **75**, 33 (1996).

[60] P. W. Fuerschbach and G. R. Eisler, Effect of laser spot weld energy and duration on melting and absorption, Sci. Technol. Weld. Joining **7**, 241 (2002).

[61] O. Perret, P. Naudy, and M. Bizouard, in *ICALEO '99 Laser Material Processing Conference* (Laser Institute of America, 1999), pp. 177–186.

[62] J. Trapp, A. M. Rubenchik, G. Guss, and M. J. Matthews, *In situ* absorptivity measurements of metallic powders during laser powder-bed fusion additive manufacturing, Appl. Mater. Today **9**, 341 (2017).

[63] S. A. David, S. S. Babu, and J. M. Vitek, Welding: Solidification and microstructure, JOM **55**, 14 (2003).

[64] J. Gockel, J. Beuth, and K. Taminger, Integrated control of solidification microstructure and melt pool dimensions in electron beam wire feed additive manufacturing of Ti-6Al-4V, Addit. Manuf. **1–4**, 119 (2014).

[65] Y. H. Xiao and G. Den Ouden, A study of GTA weld pool oscillation, Weld. J. **69**, 289 (1990).

[66] T. Klein, M. Vicanekt, J. Kroosz, I. Deckers, and G. Simon, Oscillations of the keyhole in penetration laser beam welding, J. Phys. D: Appl. Phys. **27**, 2023 (1994).